Journal of
Ceramic Science
and Technology

J. Ceram. Sci. Tech., 07 [04] 409-416 (2016)
DOI: 10.4416/JCST2016-00058
available online at: http://www.ceramic-science.com

Factors Affecting the Performance of Thermal Barrier Coatings in the Presence of V_2O_5 and Na_2SO_4

K.P. Jonnalagadda*[1], R. Eriksson[1], R.L. Peng[1], X.-H. Li[2], S. Johansson[1]

[1]IEI, Linköping University, 58183 Linköping, Sweden
[2]Siemens Industrial Turbomachinery AB, SE-61283 Finspång, Sweden

received August 12, 2016; received in revised form November 10, 2016; accepted November 21, 2016

Abstract

This study investigates the influence of temperature, salt concentration and thickness on the corrosion resistance of seven YSZ thermal barrier coatings in the presence of V_2O_5 and Na_2SO_4. For this study, a thick, high-porosity APS coating (670 μm) using hollow spherical powder (HOSP) and a thin, low-porosity APS coating (300 μm) using agglomerated and sintered (A&S) powder were fabricated. Corrosion tests were conducted at 750 °C and 900 °C with a mixture of Na_2SO_4 and V_2O_5 for four hours. At each temperature, salt concentrations of 4, 10 and 20 mg/cm^2 were used. SEM and XRD investigations after the corrosion tests revealed that a combination of low temperature and high salt concentration resulted in higher corrosion-induced damage to the thin TBC coatings. With regard to the thick TBC coatings, all except one sample failed during the corrosion test. This suggests that thick TBC coatings with higher porosity may not be suitable in corrosive environments.

Keywords: HOSP, agglomerated and sintered YSZ, hot corrosion, TBC

I. Introduction

Thermal barrier coatings (TBCs) are advanced material systems used for protecting components operating in the hot sections of a gas turbine [1–5]. The protection against the hot gas is provided by the ceramic top coat and the oxidation/corrosion resistance is provided by the intermediate bond coat deposited on top of the substrate. 7–8 wt% YSZ is the most commonly used top-coat material on account of its attractive properties. YSZ has certain limitations too, one of them being the upper operating temperature limit of 1200 °C. Above 1200 °C, YSZ transforms into yttria-poor tetragonal and yttria-rich cubic zirconia. During cooling, tetragonal zirconia transforms into monoclinic zirconia, resulting in a 3–5 % volume expansion that is sufficient to damage the mechanical integrity of the coating [6]. Spallation of the top coat is considered to be the end of life for a TBC component, and thus retaining the top coat is very important for the performance of the whole TBC.

Apart from the high-temperature operation limit, YSZ coatings are susceptible to corrosive attack from sulfur and vanadium. Sources for these corrosive species are from the intake air, which may contain a considerable amount of sodium chloride (more for turbines operating off-shore), and from the low-grade fuel, containing sulfur and vanadium, which is often used in industrial gas turbines. Considerable research has been conducted on the hot corrosion mechanism of TBCs in the presence of sodium sulfate and vanadium pentoxide [7–13]. The reactions leading to the harsh corrosion in gas turbines can be summarized in Eqs. (1) to (5).

$$2S + 3O_2 \rightarrow 2SO_3 \quad (1)$$

$$2\,NaCl + 2SO_3 + O_2 \rightarrow 2Na_2SO_4 + Cl_2 \quad (2)$$

$$4V + 5O_2 \rightarrow 2V_2O_5 \quad (3)$$

$$Na_2SO_4 + V_2O_5 \rightarrow 2NaVO_3 + SO_3 \quad (4)$$

$$ZrO_2.Y_2O_3 + 2NaVO_3 \rightarrow m\text{-}ZrO_2 + 2YVO_4 + Na_2O \quad (5)$$

$$Na_2O + V_2O_5 \rightarrow NaVO_3 \quad (6)$$

Sodium chloride reacts with sulfur and oxygen to form sodium sulfate (Eq. (2)). Vanadium reacts with oxygen, forming vanadium pentoxide (Eq. (3)). Vanadium pentoxide and sodium sulfate, when present in the ratio of 55:45 wt%, form a low-melting eutectic, sodium metavanadate ($NaVO_3$), given in Eq. (4). Reaction of YSZ with $NaVO_3$ results in the formation of YVO_4 and m-ZrO_2. The reaction byproduct, Na_2O, can react with V_2O_5 to form $NaVO_3$ [7].

Damage due to the detrimental t'-m ZrO_2 transformation was discussed above. Another contributing factor to the damage is due to YVO_4 formation that occurs as a result of yttria leaching from the top coat. YVO_4 has a rod-like structure growing in all directions, causing compressive stresses in the top coat [14]. In fact, the failure of the top coat as a result of yttria depletion caused by molten salts can be much faster compared to failure times due to sintering, thermally grown oxide (TGO) formation and

* Corresponding author: praveen.jonnalagadda@liu.se

phase transformation of t'-m ZrO_2 as a result of continuous high-temperature exposure.

The amount of YVO_4 formation and t'-m ZrO_2 transformation are considered to be dependent on the concentration and the exposure temperature. As mentioned above, the conventional top coat thickness of a TBC system is about 300 μm, which is capable of reducing the temperature over its thickness by as much as 200 – 250 °C [6, 15, 16]. Increasing the thickness of the coatings can result in a higher temperature gradient over the coating thickness. Thick thermal barrier coatings with increased thermal gradient are used in the combustion chamber of gas turbines and diesel engines. With thick TBCs, the mean combustion process temperature of, for instance, diesel engines can be increased. This extra heat can be recovered by a turbocharger or can be used in a combined cycle [17]. Nevertheless, the thick thermal barrier coatings also suffer from corrosion. As such, the performance of thick TBC coatings with high porosity during corrosion is of immense interest, but, to the best of the authors' knowledge, has not been widely reported. The aim of the present paper is to understand the influence of temperature and concentration on thick YSZ thermal barrier coatings and compare it with the conventional thin YSZ coatings.

II. Experimental

(1) Preparation of TBCs

The TBC system in this work consisted of a Hastelloy-X (Ni22Cr1.5Co0.5W9Mo18Fe1Si) substrate in the form of a disc (diameter: 25.4 mm and thickness: 5 mm). The substrates were grit-blasted with alumina particles and the bond coat, Amdry 365 – 2 (Ni23Co17Cr12Al0.2Y), was deposited by means of air plasma spraying. For spraying the top coat, two different powders were chosen. Agglomerated and sintered (A&S) powder was used to produce thin coatings with relatively low porosity. A&S powder, created by agglomeration of particulates followed by sintering for the consolidation of particulates, is one of the common powders used for producing ceramic top coats [18]. A hollow spherical powder (HOSP) was used for producing thick coatings with higher porosity. HOSP powders are prepared by passing the A&S powder over a plasma torch so the outer surface of the particle is molten, giving a smoother appearance [19].

(2) Hot corrosion tests

A mixture of V_2O_5 and Na_2SO_4 in the ratio of 55:45 (wt%) were used as corrosive salts. The salts were mixed manually and spread over the surface of the TBC sample. The TBC sample was later placed in a furnace set at 750 and 900 °C. For each temperature, salt concentrations of 4, 10, 20 mg/cm^2 were used. The samples were held at the test temperature for 4 hours, after which they were removed and allowed to cool in air. The complete test matrix is shown in Table 1. For each combination (particular concentration and temperature), one sample was used. The samples were labelled according to the powder used for spraying and the conditions tested. R for conventional A&S sprayed samples and H for HOSP samples followed by the temperature and the salt concentration used. For instance, "R750 – 4", indicates that the sample is sprayed with A&S powder and was tested at 750 °C at a concentration of 4 mg/cm^2. The corresponding condition for a HOSP sample would be then "H750 – 4". The table also indicates if the sample failed or not during the visual inspection. "P" indicates that the samples survived the corrosion test and "F" indicates that the samples failed during the corrosion test. Failure in this context is defined as cracking visible to the human eye after the corrosion tests. This is due to the fact that TBCs start to lose their functionality after spallation of the top coat. A visible crack as the failure criterion is considered relevant as it is assumed that the time taken by the coatings to spall after a visible crack appears on the surface is very short.

Table 1: Test matrix showing the different conditions under which the samples were tested and if they have survived the test. P refers to the samples that showed no damage visible to the human eye after the corrosion test and F refers to the samples that showed damage visible to the human eye and were considered failed.

	750 °C			900 °C		
Material	4 mg/cm^2	10 mg/cm^2	20 mg/cm^2	4 mg/cm^2	10 mg/cm^2	20 mg/cm^2
Agglomerated & Sintered (A&S)	*P*	*P*	*F*	*P*	*P*	*P*
Hollow Spherical Powder (HOSP)	*P*	*F*	*F*	*F*	*F*	*F*

(3) Specimen preparation and characterization

X-ray diffraction analyses using Cu-Kα radiation (wavelength: 0.154 nm) were first conducted on the corroded top surface to analyze corrosion-induced phase transformations. After the XRD analysis, the top surface was inspected in both optical and scanning electron microscopes. The samples were then infiltrated with epoxy in vacuum, cut at the cross-section and polished according to the normal routine for TBCs. Energy-Dispersive x-ray Spectroscopy (EDS) was used to determine the composition gradient of vanadium over the cross-section of the coating.

III. Results and Discussion

(1) As-sprayed microstructures

Figs. 1a – 1b show the as-sprayed cross-sections of the A&S-powder-sprayed sample with 300 μm thickness and a HOSP sample with a nominal thickness of 670 μm that is sprayed on the top of a thin A&S layer of 90 μm nominal thickness. Owing to the low thickness of the A&S sprayed layer in Fig. 1a (~ 13 % of the total thickness of A&S + HOSP), its effect on the corrosion resistance of the HOSP layer is assumed to be unaffected. Porosity analysis was performed with ImageJ and the values obtained were about 10 % for the A&S-sprayed sample and 23 – 25 % for the HOSP-sprayed sample. These pores and also cracks are inherent to APS ceramic coatings. By controlling the

powder type and the deposition parameters, it is possible to tailor these as required. Fig. 2 shows the top surface of a HOSP sample in the as-sprayed condition. Both through-splat cracks (indicated by the black arrows) and the voids (indicated by the white arrow) can be observed, which serve as pathways for molten corrosive salts.

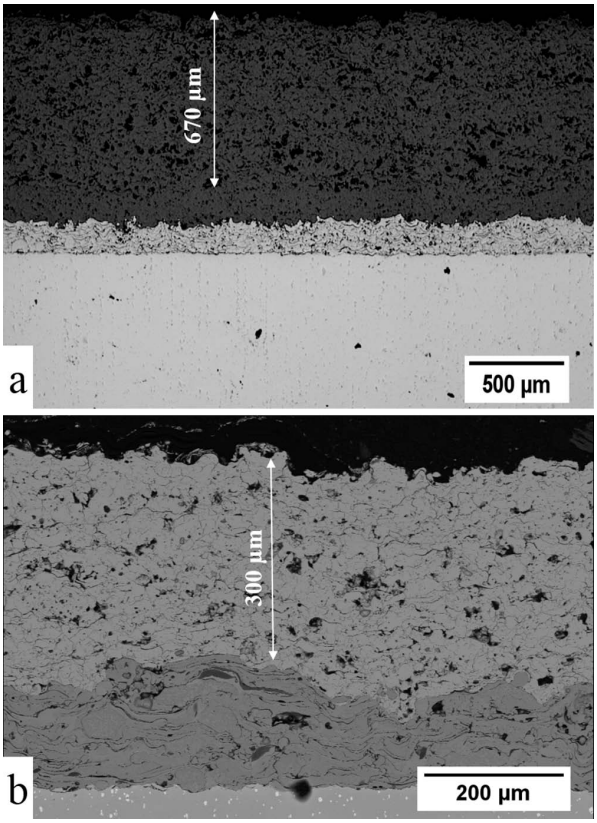

Fig. 1: Cross-section of a) HOSP as-sprayed sample, and b) A&S as-sprayed sample.

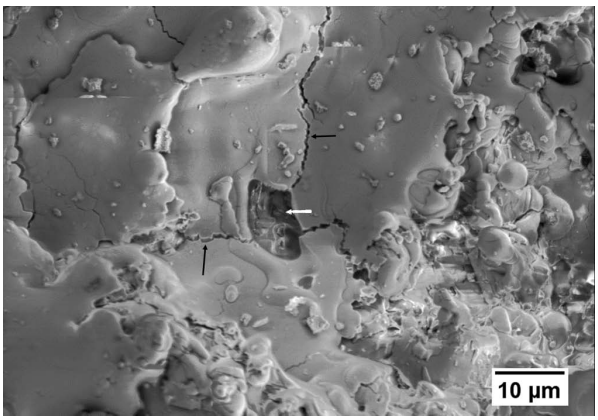

Fig. 2: Top view of the as-sprayed HOSP sample showing voids and through-splat cracks.

(2) Visual inspection of damaged samples

Figs. 3a – 3f show samples selected to illustrate typical damage on the top coat that is visible to the human eye. Figs. 3a – 3c are A&S-sprayed samples tested at 750 °C for 4 h, representing R750 – 4, R750 – 10 and R750 – 20 respectively. Figs. 3d – 3f are HOSP sprayed samples tested at 750 °C for 4 h, representing H750 – 4, H750 – 10 and H750 – 20 respectively. Increasing the salt concentration led to an increase in the corrosion-affected area in the top coat. The top coat in samples R750 – 4 (Fig. 3a) and R750 – 10 (Fig. 3b) looks undamaged while sample R750 – 20 (Fig. 3c) failed completely. In the case of the HOSP samples, H750 – 4 (Fig. 3d) showed no visible damage, H750 – 10 (Fig. 3e) showed deep cracks in the top coat and the H750 – 20 (Fig. 3f) sample showed complete top coat delamination.

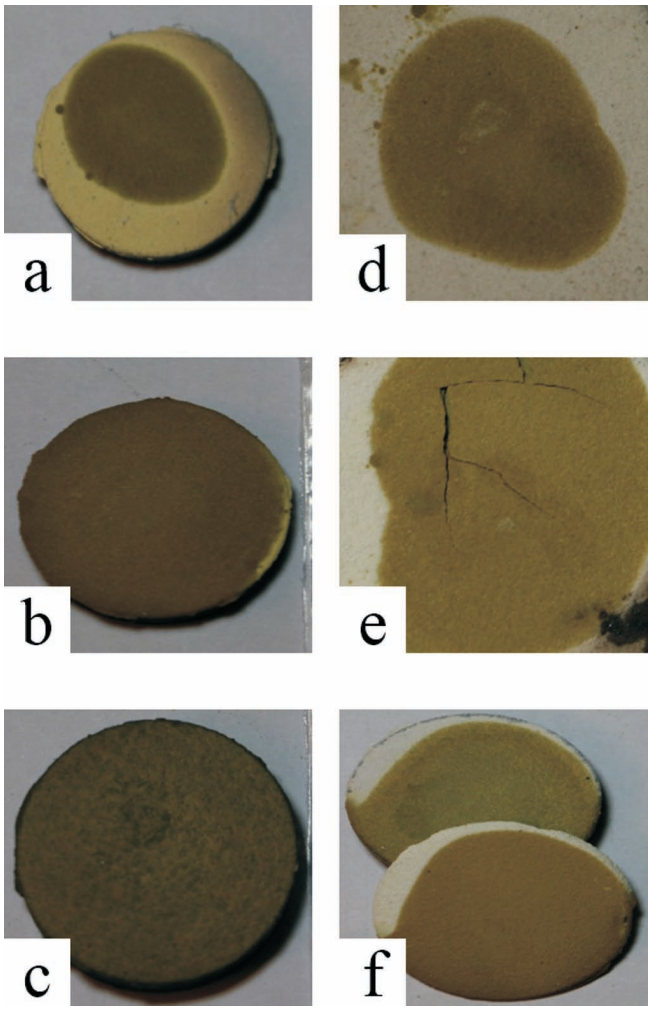

Fig. 3: Top surface after exposure to corrosion salts in a) R750 – 4, b) R750 – 10, c) R750 – 20, d) H750 – 4, e) H750 – 10, and f)H750 – 20.

(3) Mechanism of hot-corrosion-induced damage

Figs. 4a – 4e show typical images of corroded surfaces obtained from the sample H900 – 20. Molten salt, $NaVO_3$, infiltrates through the pores and microcracks in the coating and forms YVO_4, as shown in Fig. 4a, with the black arrows showing the path for the salt infiltration. EDS mapping in Fig. 4b confirms the presence of YVO_4 along the microcracks. Depending on the depth of infiltration, YVO_4 can be formed throughout the coating thickness and in turn lead to large cracks (Fig. 4c) owing to ZrO_2 phase transformation. Fig. 4d shows the representative top view of the corroded surface (the white arrow shows the corrosive product). The YVO_4 rods can penetrate from inside of the coating to the surface. The growth of these rods in the coating may result in cracks, as shown in Fig. 4e. The corrosion-induced damage is caused by the combination of stresses associated with ZrO_2 phase transformation and YVO_4 formation.

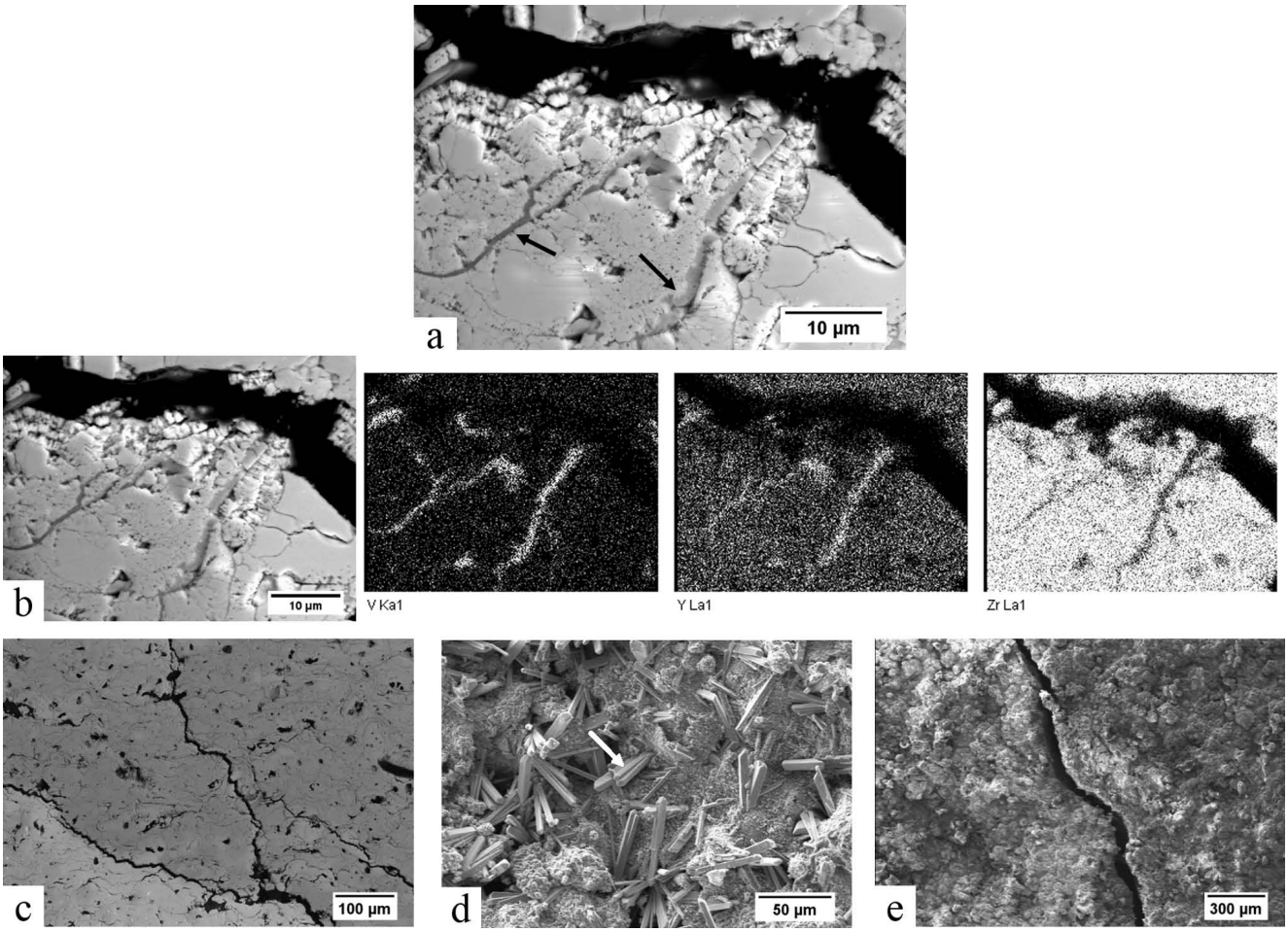

Fig. 4: a) Infiltration path for the molten salts (indicated by the black arrows), b) EDS map of (a), c) cracks in the top coat due to ZrO_2 transformation, d) top view of YVO_4 indicated by the white arrow, and e) crack due to YVO_4 formation.

The region surrounding YVO_4 is found to be m-ZrO_2 in quantitative EDS analysis, as illustrated in Fig. 5. Area 1 represents YVO_4, Area 2 represents monoclinic zirconia (yttrium content was observed to be approximately 3.2 %), Area 3 represents tetragonal prime zirconia (yttrium content was observed to be approximately 6.2 %). The Y_2O_3 content at Area 1 and 2 would then be about 4 % and 8 % respectively. From the phase diagram in Ref. [6], it can be seen that when yttria is leached from the matrix and the content is reduced from roughly 8 to 4 wt%, the microstructure shifts left towards the monoclinic structure.

(4) Influence of temperature and salt concentration

(a) *Reaction at 750 °C*

Fig. 6 shows the XRD pattern of the as-sprayed and as-corroded top surface for A&S samples exposed to 750 °C. It was observed that the only dominant phase in the as-sprayed A&S sample is t'-ZrO_2 for which the strongest peak was obtained at $2\theta = 30.2°$. A strong peak for YVO_4 was obtained at $2\theta = 25.06°$ and for m-ZrO_2 it was at $2\theta = 28.2°$ and $2\theta = 31.4°$ respectively. Thus, only the XRD pattern from $2\theta = 24 - 32°$ is shown in the figures below. As the damage occurs due to t'-m ZrO_2 transformation, it was important to analyze the phase volume fraction of m-ZrO_2 for different salt concentrations. The volume fraction of m-ZrO_2 was estimated from Eq. (7) [20].

$$M(\%) = \frac{M1 + M2}{M1 + M2 + T} \qquad (7)$$

where M is the phase volume fraction of m-ZrO_2, M1 is the peak intensity for m-ZrO_2 at (1 1) plane, M2 is the peak intensity for m-ZrO_2 at (111) plane and T is the peak intensity for t'-ZrO_2 at (101) plane. For the A&S samples with a salt concentration of 4 mg/cm^2, the volume fraction of m-ZrO_2 was approximately 46 %. When the concentration was increased to 10 mg/cm^2, the m-ZrO_2 volume fraction increased to 80 %, i.e. most of the original t' - zirconia had been transformed. For the same coating thickness but with higher salt concentration, more salts are available for reaction and hence a higher amount of phase transformation occurred. For 20 mg/cm^2, the estimation from Eq. (7) showed a lower amount of m-ZrO_2 volume fraction. This is due to the fact that the top coat had already spalled, exposing the material below which could have been less affected by corrosion. The top view of these samples is shown in Fig. 7a – 7b, which represent R750 – 4 and R750 – 10. A higher amount of YVO_4 is observed in Fig. 7b, which correlates well with the X-ray intensities for these samples (Fig. 6: R750 – 10 has higher intensity for YVO_4 than R750 – 4). Fig. 7c shows the fractured surface of the top coat. The fractured surface appears not have been much affected by the corrosion.

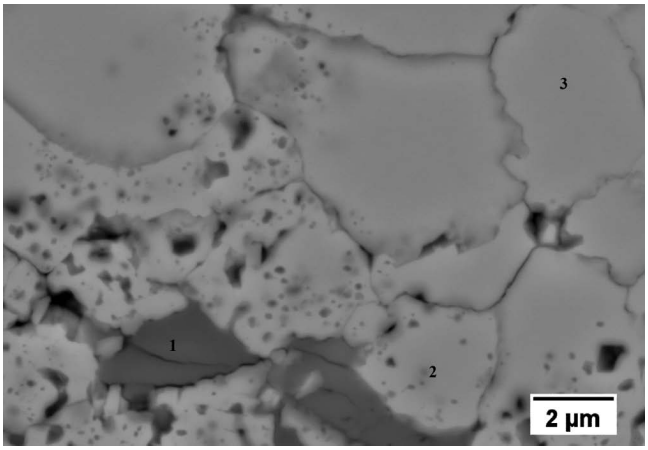

Fig. 5: Cross-section of the coating showing different areas of which (1) YVO_4, (2) m-ZrO_2, and (3) t' – ZrO_2.

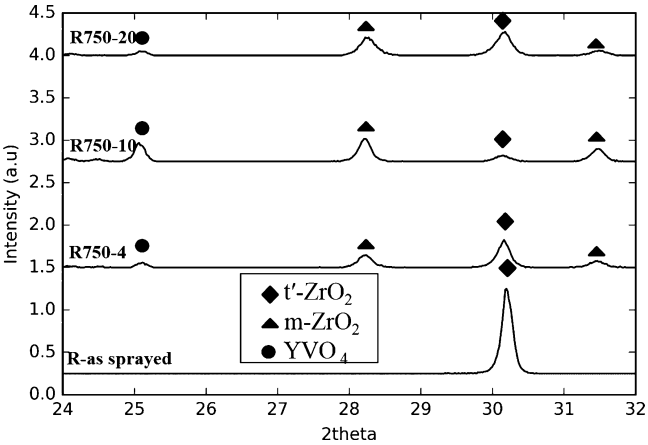

Fig. 6: XRD pattern for A&S samples tested at 750 °C with different salt concentrations.

Fig. 8 shows the XRD pattern for the HOSP sprayed samples after corrosion at 750 °C. H750 – 4 and H750 – 10 showed similar m-ZrO_2 volume fractions of roughly 45 % and 50 %. For the salt concentration of 20 mg/cm^2, the XRD results (conducted on the delaminated layer) showed about 75 % volume fraction for m-ZrO_2.

At 750 °C, Chen *et al.* [9] have observed a metastable phase, zirconium pyro vanadate ($Zr_2V_2O_7$) during their *in situ* XRD experiments. This phase is formed as a direct reaction between V_2O_5 and ZrO_2. This metastable phase subsequently decomposes into m-ZrO_2. Since the XRD analysis for the current experiment was conducted at the end of the corrosion tests, it was not possible to observe this phase. Thus, at 750 °C, as most of the V_2O_5 had been used for the reaction with ZrO_2, a smaller amount was available for forming $NaVO_3$ and hence less leaching of yttria and formation of YVO_4 occurred in comparison with the tests conducted at higher temperature(a). The corrosion-induced damage at this temperature in the top coat is due to three factors; first, due to the direct reaction between V_2O_5 and ZrO_2, which is a major factor for t'-m phase transformation; second, because of yttria leaching from YSZ, leading to ZrO_2 transformation and third, formation of YVO_4, which generates compressive stresses in the top coat.

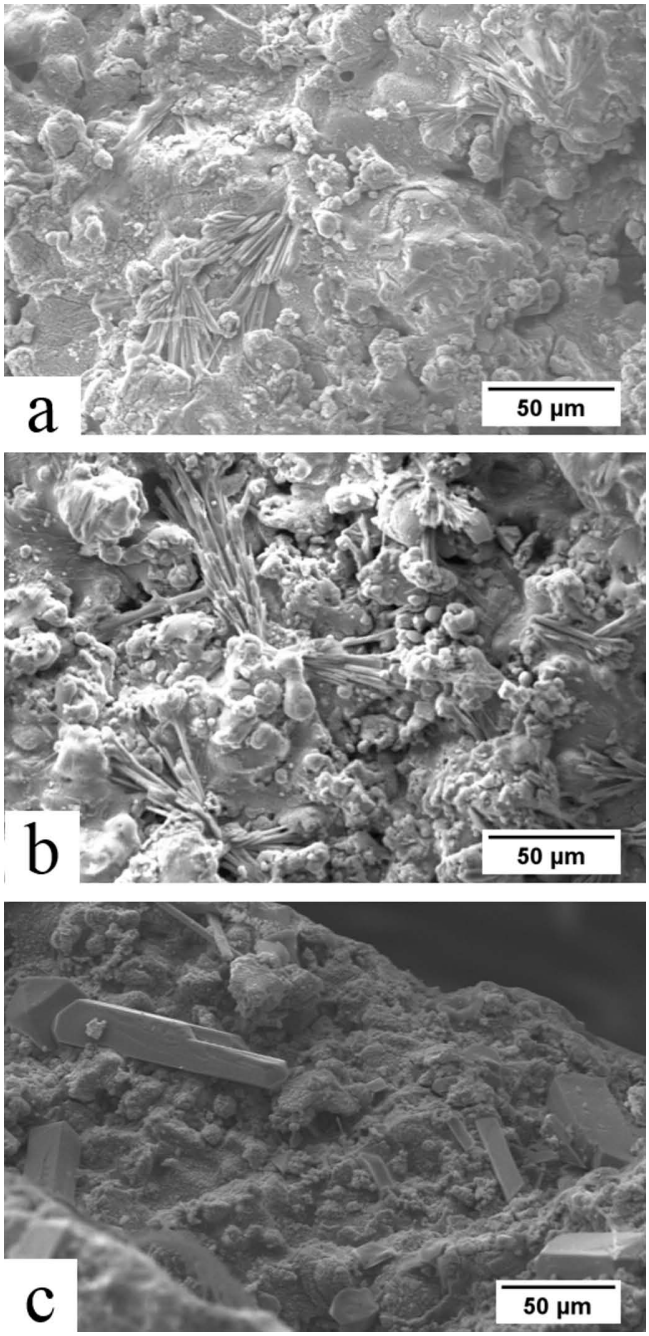

Fig. 7: Top view of the A&S samples tested at 750 °C with salt concentrations of a) 4 mg/cm^2, b) 10 mg/cm^2, and c) 20 mg/cm^2.

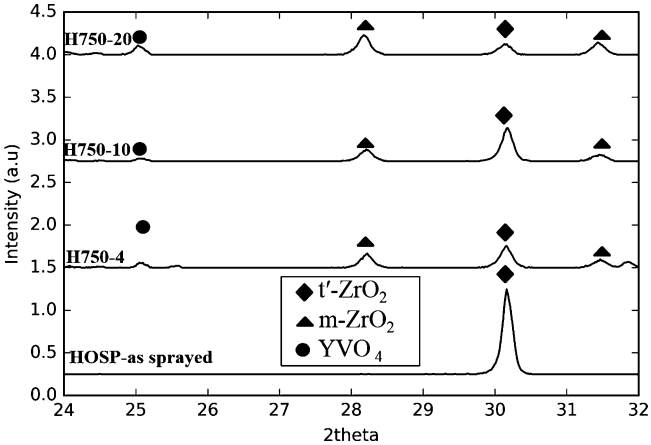

Fig. 8: XRD pattern for HOSP samples tested at 750 °C with different salt concentrations.

(b) ***Reaction at 900 °C***

A&S sprayed samples at this temperature did not show any visible damage on the top corroded surface. Fig. 9 shows the XRD pattern for A&S samples tested for three different salt concentrations. HOSP samples failed for all the salt concentrations at this temperature. For A&S sprayed sample at 4 mg/cm^2 salt concentration, the volume fraction of m-ZrO_2 was estimated to be 50 %. At salt concentrations of 10 mg/cm^2 and 20 mg/cm^2,the estimated volume fraction for m-ZrO_2 was 70 % and 90 % respectively. The intensities observed for YVO_4 with increasing salt concentrations at 900 °C are considerably higher compared to the reaction temperature of 750 °C. The reason could be that $Zr_2V_2O_7$, which exists at 750 °C, is non-existent at 900 °C [9]. This means the reaction product of V_2O_5 and Na_2SO_4, $NaVO_3$, is present in a higher amount at this temperature, hence more severe yttria leaching and, therefore, a higher amount of YVO_4. YVO_4 is formed when V_2O_5 and Y_2O_3 are present in the ratio of 50:50 mol% according to their phase diagram [21]. Phase transformation of ZrO_2 that accompanies yttria leaching should also be higher, but from Fig. 6 and Fig. 9 the intensities of t'-ZrO_2 seem to be similar for 750 °C and 900 °C. In addition, the amount of m-ZrO_2 estimated from Eq. (7) is reasonably close. The intensities of m-ZrO_2 observed at 750 °C are due to both the decomposition of $Zr_2V_2O_7$ to m-ZrO_2 and yttria leaching. The phase transformation of ZrO_2 at 900 °Cis only due to yttria depletion. Therefore, although the intensities of m-ZrO_2 appear to be similar as observed at 750 °C, higher yttria depletion had taken place at 900 °C. The corrosion-induced damage at this temperature is due to two factors only; growth stresses due to YVO_4 formation and stress due to ZrO_2 phase transformation.

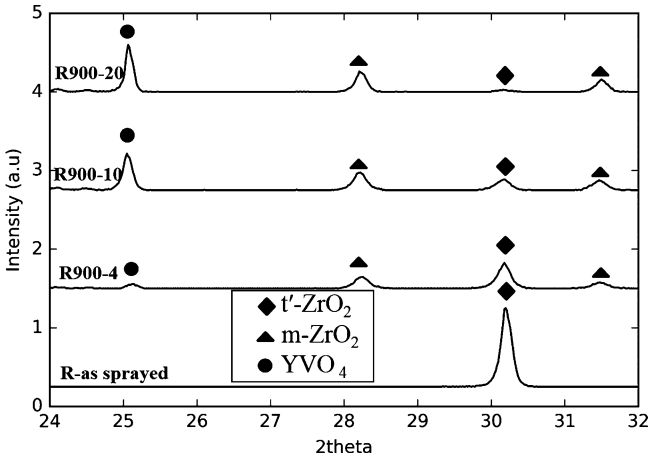

Fig. 9: XRD pattern for A&S samples tested at 900 °C with different salt concentrations.

The corrosion-induced damage is less severe at 900 °C than at 750 °C for A&S sprayed samples, as observed by human eye on the corroded surface. It is assumed that owing to the bulk transformation of ZrO_2 at 750 °C, first to $Zr_2V_2O_7$ and later to m-ZrO_2, the damage is more severe, while at 900 °C, the corrosive salts attack the zirconia stabilizer yttria, which is localized. For the HOSP samples at 900 °C, the XRD intensities were similar to the intensities observed at 750 °C. For example, Fig. 10 shows the relative intensities for the HOSP sample at 750 °C and 900 °C for the salt concentration of 10 mg/cm^2. Similar to the A&S sample, bulk transformation of zirconia takes place at 750 °C and localized attack at 900 °C. This should result in higher YVO_4 intensities at 900 °C, but they were observed to be similar at both temperatures, probably owing to the deeper penetration of the corrosive salts. As all the HOSP-sprayed samples, except one, failed during the corrosion tests it was not possible to compare the extent of damage at these two temperatures. In a comparison between the HOSP samples and the A&S samples, it was clear that HOSP samples showed poor corrosion resistance under the present experimental conditions. A possible reason for this could be easy salt penetration on account of the high porosity in the coatings. Owing to the deeper penetration of the salts, the cracks could occur throughout the coating and result in lower corrosion resistance. A&S samples with lower porosity can retard the infiltration of the corrosive salts and lead to higher corrosion resistance.

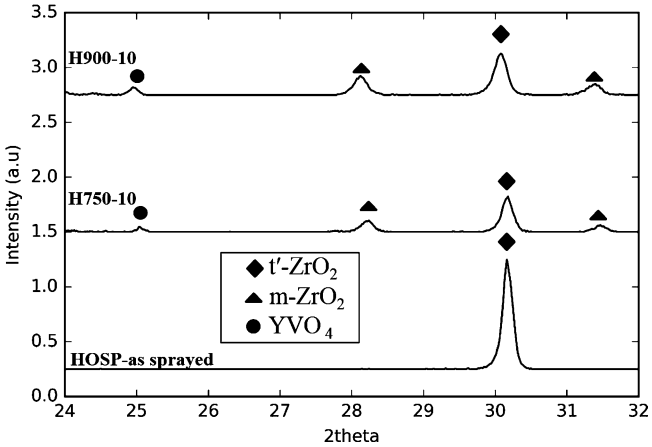

Fig. 10: XRD pattern for HOSP samples tested at 750 and 900 °C with a salt concentration of 10 mg/cm^2.

IV. Conclusions

This study on the hot-corrosion behavior of air-plasma-sprayed YSZ enables further understanding of the factors influencing the overall corrosion-induced damage in the presence of V_2O_5 and Na_2SO_4. For an agglomerated and sintered sprayed sample, the damage is more severe at 750 °C compared to 900 °C. Three factors were observed that contribute to corrosion-induced damage at 750 °C: direct reaction between V_2O_5 and ZrO_2, growth stresses owing to YVO_4 formation and accompanying stress due to t'-m ZrO_2 transformation. At 900 °C, the contribution to corrosion-induced damage is due to YVO_4 formation and t'-m ZrO_2 transformation. An increase in salt concentration led to an increase in YVO_4 and m-ZrO_2 intensities and reduced t'-ZrO_2 intensity. A combination of low temperature and high salt concentration leads to severe corrosion-induced damage as observed in A&S-sprayed samples. For the HOSP-sprayed samples, this trend could not be confirmed as all the samples except one failed during the corrosion tests. Nevertheless, this suggests that thicker porous coatings may not be suitable for corrosive environments.

Acknowledgement

The authors gratefully acknowledge the funding for this research from Vinnova, Sweden.

References

1 Padture, N.P., Gell, M., Jordan, E.H.: Thermal barrier coatings for gas-turbine engine applications, *Science.*, **296**, 280 – 284, (2002).

2 Gleeson, B.: Thermal barrier coatings for aeroengine applications, *J. Propul. Power.*, **22**, 375 – 383, (2006).

3 DeMasi-Marcin, J.T., Gupta, D.K.: Protective coatings in the gas turbine engine, *Surf. Coat. Tech.*, **68 – 69**, 1 – 9, (1994).

4 Goward, G.W.: Progress in coatings for gas turbine airfoils, *Surf. Coat. Tech.*, **108 – 109**, 73 – 79, (1998).

5 Pomeroy, M.J.: Coatings for gas turbine materials and long term stability issues, *Mater. Des.*, **26**, 223 – 231, (2005).

6 Bose, S.: High temperature coatings. Butterworth-Heinemann., Oxford, 2007.

7 Habibi, M.H., Wang, L., Guo, S.M.: Evolution of hot corrosion resistance of YSZ, $Gd_2Zr_2O_7$, and $Gd_2Zr_2O_7$ + YSZ composite thermal barrier coatings in Na_2SO_4 + V_2O_5 at 1050 °C, *J. Eur. Ceram. Soc.*, **32**, 1635 – 1642, (2012).

8 Abubakar, A.A., Akhtar, S.S., Arif, A.F.M.: Phase filed modelling of V_2O_5 hot corrosion kinetics in thermal barrier coatings, *Comp. Mater. Sci.*, **99**, 105 – 116, (2015).

9 Chen, Z., Speakman, S., Howe, J., Wang, H., Porter, W., Trice, R.: Investigation of reactions between vanadium oxide and plasma-sprayed yttria-stabilized zirconia coatings, *J. Eur. Ceram. Soc.*, **29**, 1403 – 1411, (2009).

10 Park, S.Y., Kim, J.H., Kim, M.C., Song, H.S., Park, C.G.: Microscopic observation of degradation behavior in yttria and ceria stabilized zirconia thermal barrier coatings under hot corrosion, *Surf. Coat. Tech.*, **190**, 357 – 365, (2005).

11 Jones, R.L.: Some aspects of the hot corrosion of thermal barrier coatings, *J. Therm. Spray Techn.*, **6**, 77 – 84, (1997).

12 Yugeswaran, S., Kobayashi, A., Ananthapadmanabhan, P.V.: Initial phase hot corrosion mechanism of gas tunnel type plasma sprayed thermal barrier coatings, *Mater. Sci. Eng.*, *B*, **177**, 536 – 542, (2012).

13 Jamali, H., Mozafarinia, R., Shoja-Razavi, R., Ahmadi-Pidani, R.: Comparison of hot corrosion behaviors of plasma-sprayed nanostructured and conventional YSZ thermal barrier coatings exposure to molten vanadium pentoxide and sodium sulphate, *J. Eur. Ceram. Soc.*, **34**, 485 – 492, (2014).

14 Saremi, M., Keyvani, A., Sohi, M.H.: Hot corrosion resistance and mechanical behavior of atmospheric plasma sprayed conventional and nanostructured zirconia coatings, *Int. J. Mod. Phys. Conf. Ser.*, **05**, 720 – 727, (2012).

15 Reed, R.C.: The superalloys. Cambridge University Press., Cambridge, 2006.

16 Belmonte, M.: Advanced ceramic materials for high temperature applications, *Adv. Eng. Mater.*, **8**, 693 – 703, (2006).

17 Ahmaniemi, S., Vippola, M., Vuoristo, P., Mäntylä, T., Cernuschi, F., Lutterotti, L.: Modified thick thermal barrier coatings: microstructural characterization, *J. Eur. Ceram. Soc.*, **24**, 2247 – 2258, (2004).

18 Davis, J.R.: Handbook of thermal spray technology. ASM International, Ohio, 2004.

19 Dorfman, M.R., Correa, L.F., Dambra, G., Laul, K., Schmid, R.K.: Method of producing a pre-alloyed stabilized zirconia powder. U.S. Patent Application 0,107,580, (2004).

20 Keyvani, A., Saremi, M., Sohi, M.H.: Microstructural stability of zirconia-alumina composite coatings during hot corrosion test at 1050 °C, *J. Alloy. Compd.*, **506**, 103 – 108, (2010).

21 Levin, E.M.: The system Y_2O_3-V_2O_5, *J. Am. Ceram. Soc.*, **50**, 381 – 382, (1967).